Technical Report

TR-2008-019

A framework for geometric analysis of vascular structures: Applications to cerebral aneurysms

by

Marina Picinelli, Alessandro Veneziani, David A. Steinman, Andrea Remuzzi, Luca Antiga

MATHEMATICS AND COMPUTER SCIENCE

EMORY UNIVERSITY

A framework for geometric analysis of vascular structures: applications to cerebral aneurysms

Marina Piccinelli, Alessandro Veneziani, David A. Steinman,
Andrea Remuzzi and Luca Antiga*

***Abstract*—There is a well documented evidence that vascular geometry has a major impact in blood flow dynamics and consequently in the development of vascular diseases, like atherosclerosis and cerebral aneurysmal disease. The study of vascular geometry and the identification of geometric features associated with a specific pathological condition can therefore shed light into the mechanisms involved in the pathogenesis and progression of the disease. Although the development of medical imaging technologies is providing increasing amounts of data on the three-dimensional morphology of the in-vivo vasculature, robust and objective tools for quantitative analysis of vascular geometry are still lacking.**

In this paper, we present a framework for the geometric analysis of vascular structures, in particular for the quantification of the geometric relationships between the elements of a vascular network based on the definition of centerlines. The framework is founded upon solid computational geometry criteria, which confer robustness of the analysis with respect to the high variability of in-vivo vascular geometry. The techniques presented are readily available as part of the Vascular Modeling Toolkit (VMTK), an open source framework for image segmentation, geometric characterization, mesh generation and computational hemodynamics specifically developed for the analysis of vascular structures.

As part of the Aneurisk project, we present the application of the present framework to the characterization of the geometric relationships between cerebral aneurysms and their parent vasculature.

***Index Terms*—3D Modeling, Vascular Geometry, Geometric Quantification, Cerebral Aneurysms**

I. INTRODUCTION

THERE is a well documented evidence that vascular geometry has a major impact in the blood dynamics and, in turn, in the origin and development of vascular disease, through the action of forces exerted by flowing blood on the vascular wall. [1]–[4]. Typical examples of these relationships are the development of atherosclerotic lesions [5], [6] and the formation of intracranial aneurysms preferentially at bifurcations and sharp bends [7], [8].

The study of vascular geometry in relation to the development of specific pathologic conditions can therefore shed light on the hemodynamic triggers involved in the pathogenesis and in the progression of the disease [9], [10]. Furthermore, the identification of geometric quantities that are associated to a specific pathological condition, or that have some predictive power with respect to the severity of disease progression is a valuable endeavor in itself. In fact, a geometric quantity which is a surrogate of a specific flow condition is amenable for inclusion in a large-scale clinical trial and, once validated, it is directly usable as a clinical criterion.

The recent development of medical imaging devices, such as rotational angiography (RA), computed tomography (CT) and magnetic resonance (MR), has lead to the availability of large amounts of data on the three dimensional (3D) morphology of the in-vivo vasculature, for the investigation of these aspects for diagnostic and prognostic purposes [11]–[15]. Still, a quantitative analysis of the relationship between vascular geometry and arterial physiopathology is made difficult by the large variability of real anatomies on one hand, and by the objective difficulty in retrieving quantitative data from images in a robust, operator-independent way on the other.

In this paper, we present a framework devised for 3D modeling and geometric characterization of vascular structures, readily available in the *Vascular Modeling Toolkit* (VMTK) [16], and we show how it can be employed for the characterization of cerebral aneurysms in relation to their parent vasculature. In particular, after a quick glance to image segmentation (Sect. II), we focus our attention on centerline calculation (Sect. III) and bifurcation identification and quantitative characterization (Sect. IV). Centerline of a vessel is in general a significant synthesis of basic features of a vessel (in terms of curvature, torsion, tortuosity), and however its definition from a general 3D surface is not trivial. Some techniques for a robust computation of the centerline based on the concept of Voronoi diagram are presented here. As already pointed out, bifurcations are in general an interesting part of the vascular tree, quite often preferential site of atherosclerotic plaque development or aneurysm growth. Robust geometric characterization of bifurcations potentially plays an important role in understanding pathogenesis and disease progression. In Sect. V we illustrate examples of application of the present framewotk to the case of middle cerebral artery and internal carotid artery aneurysms. Medical images have been obtained in the context of the Aneurisk project, a collaborative research project aimed at assessing the role of geometry and hemodynamics in the development and rupture of cerebral aneurysms.

Manuscript received October 1, 2008; revised ...

M. Piccinelli is with Department of Mathematics and Computer Science, Emory University, Atlanta (GA) USA and Biomedical Engineering Department, Mario Negri Institute for Pharmacological Research, Bergamo, Italy.

A. Veneziani is with Department of Mathematics and Computer Science, Emory University, Atlanta (GA) USA. USA.

D. A. Steinman is with Department of Mechanical and Industrial Engineering, University of Toronto, Canada.

A. Remuzzi is with Biomedical Engineering Department, Mario Negri Institute for Pharmacological Research, Bergamo, Italy, and Industrial Engineering Department, University of Bergamo, Italy.

L. Antiga is with Biomedical Engineering Department, Mario Negri Institute for Pharmacological Research, Bergamo, Italy (e-mail: antiga@marionegri.it).

II. IMAGE SEGMENTATION

The first step in our framework consists in building a geometric representation of a vascular network from imaging data, operation referred to as image segmentation. The goal is to reliably identify the surface corresponding to the boundary between the lumen and the vascular wall. Assuming that for the given imaging modality blood has a different intensity compared to the vessel wall and surrounding tissue (this is the case for contrast-enhanced RA, CT and MR), the lumen boundary can be assumed to be located at the locations of maximal intensity transition from the lumen to the outside. Following this basic assumption, we locate the lumen boundary where the magnitude of the gradient of image intensity $I(\mathbf{x})$, where $\mathbf{x}$ is the vector of space coordinates, has a ridge (see Figure 1A and 1B).

The segmentation process is carried out with the use of implicit deformable models, whose deformation under image-based forces is described using the level set technique [17]–[19]. The surface of the vascular model S is represented as the iso-surface of level $k = 0$ of a time-dependent function $\Phi(\mathbf{x}, t)$ fulfilling an appropriate differential equation driven by the image-based forces. In particular, we employ

$$\frac{\partial \Phi}{\partial t} = w_2 \nabla \cdot \left(\frac{\nabla \Phi}{|\nabla \Phi|} \right) \nabla \Phi - w_3 \nabla \cdot |\nabla I| \nabla \Phi \tag{1}$$

where w_2, w_3 are user-defined parameters [19]. The first term on the right hand side has the role of curvature regularization and the section is an advective term with the role of attracting the 0-level set of Φ to the ridges of the gradient magnitude (Figure 1). Equation (1) needs to be properly completed by boundary and initial conditions. In particular, the method yields accurate results when the initial condition is such that the 0-level set of Φ is close enough to the target surface. In our case, we resort to the following initialization method, referred to as *Colliding Fronts algorithm*.

1) The user selects two seed points P_1 and P_2 interactively on the 3D image. Let us denote by $T_i(\mathbf{x}) (i = 1, 2)$ the travel time of a wave originating from P_i and traveling with velocity $I(\mathbf{x})$, i.e. faster where the intensity is brighter (as it typically is the case within the lumen). Assuming that $T_i(P_i) = 0$, the fields $T_i(\mathbf{x})$ are constructed to satisfy the Eikonal equation for $i = 1, 2$:

$$|\nabla T_i(\mathbf{x})| = \frac{1}{I(\mathbf{x})}. \tag{2}$$

2) The quantity

$$\varphi_0 = \nabla T_1 \cdot \nabla T_2$$

is computed, which is negative where the two waves travel in opposite directions and positive when they travel in the same direction. This property can therefore be used for identifying the region comprised between the two seed points. In addition, since I drives the velocity propagation of the waves, these are assumed to significantly slow down in correspondence of the lumen boundary, so that φ_0 becomes positive. Therefore, the isosurface $\varphi_0 = 0$ is in general a good approximation of the lumen boundary in the region of interest between the seed points. Last, $\varphi_0 = 0$ automatically excludes side branches, because the two fronts seep into a side branch traveling in the same direction.

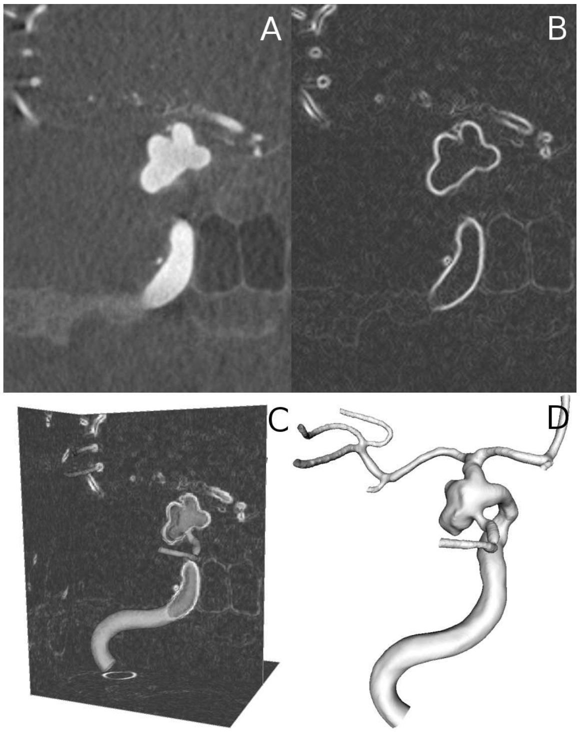

Fig. 1: Level set segmentation principles: A. image data obtained from 3D rotational angiography (RA) of an internal carotid artery bearing an aneurysm; B. gradient magnitude of image intensity; C. location of the level set model with respect to the ridges of the gradient magnitude; D. the final 3D surface model.

It is worth pointing out that the purpose of the Colliding Fronts algorithm is to provide a flexible way to selectively initialize a surface close enough to the gradient magnitude ridges that the inflation stage, normally required for deformable model-based approaches, is not needed, since the surface is already within the capture region of the advection term. This confers robustness to the localization of the position of the lumen boundary while retaining flexibility in the choice of the segmented regions. In Figures 2, A, B and C we illustrate the initialization steps for a single vascular segment. Thanks to the implicit representation of the surface provided by the level set formulation, different tracts can be merged in successive steps so to obtain a complete vascular network.

Notice that although the results presented in the sequel are based on RA images, this segmentation technique can be applied to images obtained with different imaging modalities (CT or MR). Moreover, we point out that the geometric characterization of the vessel discussed in the subsequent paragraphs is independent of the specific segmentation technique adopted and can be applied to any piecewise linear representation of a 3D surface representing a vascular network.

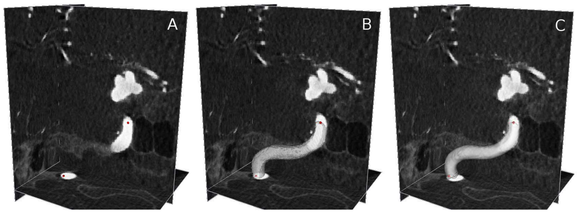

Fig. 2: Level set initialization using the Colliding Fronts algorithm: A. positioning of two seeds on the 3D image for the identification the vascular branch of interest; B. initial surface generated with the Colliding Fronts algorithm; C. the final level set model of the selected vascular tract.

III. COMPUTATION OF THE CENTERLINES

Geometric analysis and synthesis of a vascular tree is in general a challenging task, both for the extreme anatomical variability of in-vivo morphologies and for the availability of many potential quantities of interest. By exploiting the tubular structure of vessels, a reasonable approach is to resort to the concept of *centerline*. Although this is an intuitive geometric entity, its formal definition is challenging especially at sites where vascular segments exhibit a non tubular morphology, such as at bifurcations.

We define *centerline* the line between two sections of the lumen, whose minimal distance from the boundary is maximal in some sense. Consequently, centerline computation can be formally described as a functional minimization problem. If s is the curvilinear abscissa along a curve $\mathbf{c}(s)$ connecting the generic points $\mathbf{p}_0$ and $\mathbf{p}_1$, corresponding to the values s_0 and s_1 respectively, we look for the curve $\mathbf{c}(s)$, such that the functional

$$E(\mathbf{c}(s)) \equiv \int_{s_0}^{s_1} G(\mathbf{c}(s))ds \tag{3}$$

is minimal, with $\mathbf{c}(s) \in \mathcal{R}^3$, $G(\cdot)$ being a cost-density function to be properly constructed.

A method for the selection of G based on the concepts of *medial axis, Voronoi diagram* and *wave propagation*, was presented in a previous work [19]. Given the importance of these concepts in the foundations of the present framework, we briefly recall the theory behind the definition of the functional in Equation (3).

Let $\Omega \in R^3$ be a volume with boundary $\partial\Omega$. For any point in $\mathbf{x} \in \Omega$, we indicate with $DT(\mathbf{x})$ the minimal distance of $\mathbf{x}$ from the boundary, i.e.

$$DT(\mathbf{x}) \equiv \min_{\mathbf{y}\in\partial\Omega} ||\mathbf{x} - \mathbf{y}||$$

being $||\cdot||$ the Euclidean distance. In other words, $DT(\mathbf{x})$ is the radius of the sphere centered in $\mathbf{x}$ and tangential in at least a point of $\partial\Omega$. Moreover, we define a *maximal inscribed sphere* a sphere inscribed in $\partial\Omega$ which is not entirely contained in any other inscribed sphere. The *Medial axis* $MA(\Omega)$ is a surface given by the locus of the centers of maximal inscribed spheres in Ω. This is actually a non-manifold surface contained in Ω and dual to $\partial\Omega$. In principle, once $\partial\Omega$ is known, $MA(\Omega)$ can be retrieved. In practice, this is a challenging task, and approximation procedures are required. A classical approximation method for discrete surfaces relies on the concept of *Voronoi diagram*, defined as follows [20], [21].

Let P be a set of points on $\partial\Omega$ and $\mathbf{p}$ be a point in P. The Voronoi region $V(\mathbf{p})$ associated with $\mathbf{p}$ is defined as the region in $\mathcal{R}^3$ whose points are closer to $\mathbf{p}$ than to any other point of P, i.e.

$$V(\mathbf{p}) \equiv \left\{\mathbf{x} \in R^3 : ||\mathbf{p} - \mathbf{x}|| \leq ||\mathbf{q} - \mathbf{x}||, \qquad \forall \mathbf{q} \in P\right\}. \tag{4}$$

Given a point set P in $\mathcal{R}^3$, the union of the Voronoi regions $V(P)$ constitutes a tessellation of all $\mathcal{R}^3$. The collection $Vor(P)$ of the boundaries of the Voronoi regions for any point in P is called *Voronoi diagram*.

If we define $DT_P(\mathbf{x}) \equiv \min_{\mathbf{y}\in P} ||\mathbf{x} - \mathbf{y}||$ as the counterpart of $DT(\cdot)$ when this is computed only with respect to the set P, then the Voronoi diagram coincides with the surface collecting the ridges of $DT_P(\mathbf{x})$. In this respect, the Voronoi diagram can be considered a sort of *finite dimensional approximation* of the medial axis. In our framework, the Voronoi diagram is computed by resorting to its dual, the Delaunay tessellation of P, denoted by $Del(P)$. The latter is a tetrahedral reticulation of the point set P, where the sphere circumscribed to each tetrahedron does not strictly contain any other point of P. It is possible to prove that the vertices of the Voronoi diagram correspond to the circumcenters of Delaunay tetrahedra, and that the connectivity of the tessellation allows to compute the connectivity of the Voronoi diagram, since Voronoi vertices are connected by an edge if the corresponding Delaunay tetrahedra share a face. However, since the Delaunay tessellation of a point set produces a strictly convex tetrahedralization, tetrahedra located outside the surface have to be removed before the Voronoi diagram can be computed, as we are only interested in the approximation of MA inside the domain of interest. The removal of the non-internal tetrahedra from the Delaunay tessellation is carried out by removing tetrahedra having circumcenter laying outside Ω, more formally

$$(\mathbf{p}_j - \mathbf{c}) \cdot \mathbf{n}_j < 0, \quad j = 1, 2, 3, 4$$

where $\mathbf{p}_j$ are the vertices a tetrahedron, $\mathbf{c}$ its circumcenter and $\mathbf{n}_j$ is the outward normal vector to the surface defined at $\mathbf{p}_j$. After removal, *internal* or *embedded Voronoi diagram* $Vor_I(P)$ is defined from the Voronoi polygons whose connectivity is complete.

Figure 3 A and B illustrates $Vor_I(P)$ for a portion of cerebral vasculature. The internal Voronoi diagram is a non-manifold surface composed by convex polygons whose vertices are the centers of maximal inscribed spheres, which coincide with the circumspheresof the associated Delaunay tetrahedra. The maximal inscribed sphere radius (MISR), hereafter denoted by $R_M(\mathbf{x})$, is associated with each vertex, providing information on the distance from the boundary. Notice that the spheres featuring a large radius (whose centers are in the deeper portion of the Voronoi diagram) are associated to the basic features of the geometry, while the small-scale details are typically captured by small spheres, with centers are located on the outer portions of the Voronoi diagram.

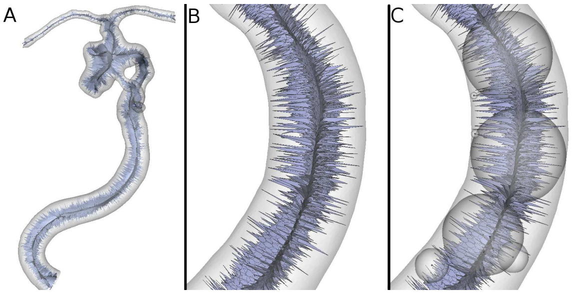

Fig. 3: A. Internal Voronoi diagram of the 3D model of an internal carotid artery bearing an aneurysm; B and C. details of the Voronoi diagram as a non-manifold surface composed of convex polygons, whose vertices are the centers of maximal inscribed spheres; the larger spheres are associated with basic features of the geometry and the smaller spheres capture the small-scale details of the model surface.

At this point, we define the centerline $\mathbf{c}(s)$ as the result of the minimization of the functional in Equation (3) taking $\mathbf{c}(s) \in Vor_I(P)$, i.e. the domain where $\mathbf{c}(s)$ is looked for is restricted from $\mathcal{R}^3$ to $Vor_I(P)$, i.e. and the function $G(\cdot)$ is defined as

$$G(\mathbf{x}) = \frac{1}{R_M(\mathbf{x})}, \qquad \forall \mathbf{x} \in Vor_I(P).$$

This way, $\mathbf{c}(s)$ is guaranteed to be medial, since it sits on top of the Voronoi diagram, and minimizes the line integral of the inverse of the MISR, i.e. it tends to the deeper portions of the Voronoi diagram (for this reason, such defined $G(\cdot)$ is referred to as *centering potential*).

In practice, this minimization problem is recast into a minimal cost path problem solved by first finding a solution to the eikonal equation

$$|\nabla\tau(\mathbf{x})| = G(\mathbf{x}), \qquad \forall \mathbf{x} \in Vor_I(P)$$

where $\tau(\mathbf{x})$ are the arrival times of a wave traveling on the Voronoi diagram with speed $R_M(\mathbf{x})$, with initial condition $\tau(\mathbf{p}_0) = 0$. Algorithmically, the solution is obtained using the Fast Marching Method [17] extended to non-manifold surfaces. Figure 4 shows the embeeded Voroni diagram and the Eikonal solution plotted in $Vor_I(P)$, where P is the point set of the vertices of the triangulated surface representing the lumen. The centerline is finally computed by tracing the path from $\mathbf{p}_1$ back to $\mathbf{p}_0$ on $Vor_I(P)$ along the direction of steepest descent of $\tau(\mathbf{x})$.

One of the potential drawbacks of resorting to Voronoi diagrams for obtaining synthetic shape descriptors is its sensitivity to surface noise. Several algorithms for the extraction of a *stable* subset of the Voronoi diagram have been proposed in the literature [22]. It is however worth noting that in our case noise affects principally peripheral Voronoi elements, while the deeper ones, which are targeted by our application, are less sensitive to small changes in the shape of the surface. For this reason, in our framework we work directly on the entire Vor_I diagram. As an example, in Figure 5 we show two models for the same vascular network. The former is obtained using the segmentation approach presented in this paper, the latter is obtained by extraction of an intensity isosurface from the original images. The associated Voronoi diagrams are shown together with the surfaces. Notice that, even if the second surface presents a larger amount of noise, the two centerlines extracted do not exhibit significant differences between the two models. Besides robustness, another advantange of this approach is that centerlines are well defined even in presence of non-tubular shapes, such as bifurcations and saccular aneurysms, as shown in Section V.

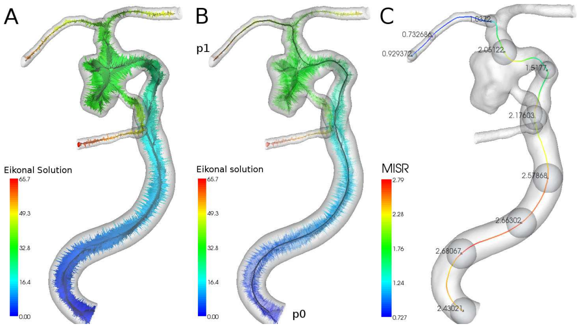

Fig. 4: A. Voronoi diagram color-coded with the solution of the Eikonal equation; B. computation of the centerline path between the endpoints; C. final centerline: each point is associated with the radius of maximal inscribed spheres (MISR).

A. Tube functions and surfaces

The union of the maximal inscribed spheres whose centers lie on the centerline defines a scalar function $\theta : \mathcal{R}^3 \rightarrow \mathcal{R}$, the *tube function*, as follows

$$\theta_{\mathbf{c},r}(\mathbf{x}) = \min\left[|\mathbf{x} - \mathbf{c}(s)|^2 - r^2(s)\right], \qquad s \in [s_0, s_1] \quad (5)$$

$\mathbf{c}$ being a generic point on the centerline and r the corresponding maximal inscribed sphere radius. The zero isosurface of $\theta_{\mathbf{c},r}(\mathbf{x})$ is referred to as tube, or canal surface. The tube function is negative inside its surface. As shown in Figure 6, the tube surface for a vascular segment is by construction strictly contained into the lumen – a *maximal inscribed tube*, with slight abuse of terminology [23].

There is a connection between the local radius of a tube surface and the radiological convention for measuring the diameter of a vessel. In fact, the diameter of a vessel is evaluated as the minimum diameter measured over a range of lateral projections. Figure 6 B shows that there is always a projection in which the tube surface is tangential to the model, so that the vessel size, or the degree of a stenosis, is reflected by the radius of the tube surface.

Tube functions will play an important role in the remainder of this paper, as they constitute the fundamental building blocks of our geometric characterization framework.

B. Geometric characterization of centerlines

Since centerlines are lines in space it is possible to proceed with their geometric characterization based on classical differential geometry of curves. In particular, we consider *curvature*,

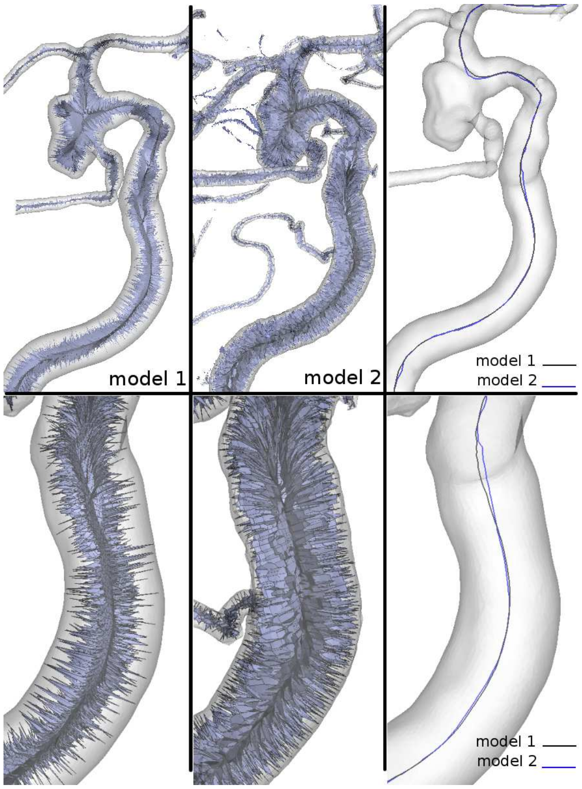

Fig. 5: Comparison of the internal Voronoi diagram and the centerlines of two models obtained for the same image data: model 1 is obtained using level set segmentation, model 2 is obtained using iso-surface extraction on the original 3D image, presenting a higher degree of surface noise; details of the internal Voronoi diagrams and of the centerlines are shown in the lower portion of the image.

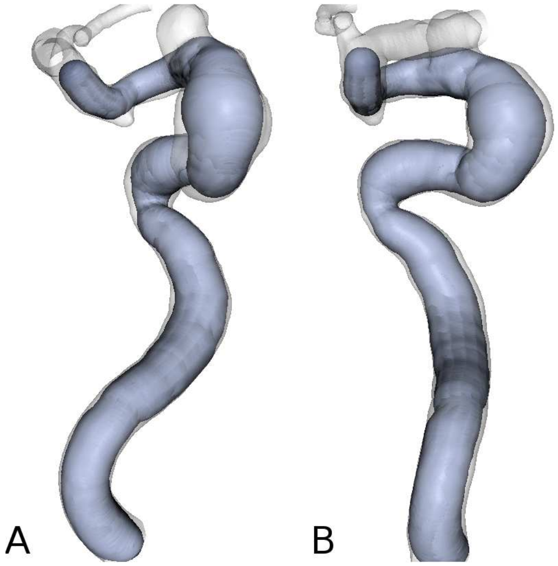

Fig. 6: Tube surface of the internal carotid artery: the surface is strictly contained into the lumen; from the two projections it can be noted that there is always a projection in which the tube surface is tangent to the model, connecting tube radius to the radiological convention for measuring vessel diameters.

torsion, *tortuosity* as relevant quantities for the characterization of a vascular segment, since they have been demonstrated to be potentially linked to specific hemodynamic patterns [1], [9], [24] and disease processes [10], [25]–[27]. Using similar differential geometry concepts, we then face the problem of defining local reference frames along the centerlines, which will serve as building blocks for comparative geometric analysis as presented in the following sections.

Before proceeding, let us first introduce a parametrization of the line through the associated *curvilinear abscissa*. After this operation, the line is reparameterized by means of the variable $s \in [0, L]$, where L is the arc length of the centerline. The abscissa ranges over the 3D course of the centerline and relates every point to its Euclideian distance from a point assumed to be the origin, denoted by $\mathbf{p}_0 = \mathbf{c}(0)$.

1) Curvature: Curvature (or more precisely *extrinsic curvature*) of the line $\mathbf{c}(s)$, is defined as

$$\kappa(s) = \frac{|\mathbf{c}\prime(s) \times \mathbf{c}\prime\prime(s)|}{|\mathbf{c}\prime(s)|^3}, \tag{6}$$

and measures the deviation of the curve from a straight line.

Since centerlines are guaranteed to be only C0 continuous, differentiation, here and in the following, is performed using finite differences on a smoothed representation of the centerline, obtained using a Laplacian filter to get rid of spurious high-frequency noise. Note that this procedure is only employed for the computation of derivatives with respect to the parametric coordinate. An alternative, recently presented approach, is to use *free-knots regression splines* to generate a high-order continuous representation of the curve, which allows for analytic computation of derivatives [28].

At a given point $\mathbf{c}(\bar{s})$, curvature is the inverse of the radius of the *osculating circle*. i.e. the circle that approximates the curve (i.e. has a second-order contact with the curve) in $\mathbf{c}(\bar{s})$. The plane identified by the osculating circle is commonly referred to as *osculating plane*. $\kappa(s)$ is always positive, and it vanishes on rectilinear portions of the line.

2) Torsion: As curvature measures the deviation of the curve from a straight line, so torsion measures its local deviation from lying on the osculating plane, or, equivalently, how sharply the line is twisting in space.

Considering a parameterized curve with non vanishing curvature, the torsion reads

$$\tau(s) = \frac{[\mathbf{c}\prime(s) \times \mathbf{c}\prime\prime(s)] \cdot \mathbf{c}(s)\prime\prime\prime}{|\mathbf{c}\prime(s) \times \mathbf{c}(s)|} \tag{7}$$

Torsion reflects the rate of rotation of the osculating plane around the curve in the neighborhood of a point. Sign of $\tau(s)$ distinguishes between clockwise or counter-clockwise rotations of the osculating plane.

3) Tortuosity: Given the length L of the centerline and the Euclidean distance between its end-points D, tortuosity is defined as

$$\chi = \frac{L}{D} - 1. \tag{8}$$

Tortuosity is the percentage increment in the length of a curve deviating from a rectilinear line.

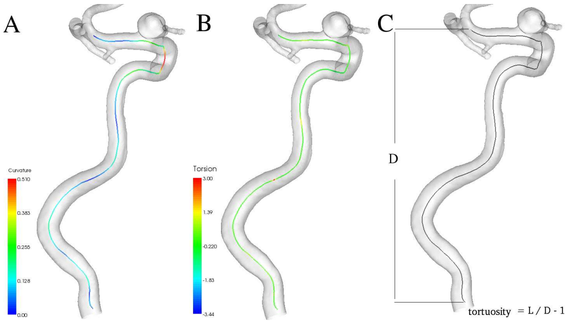

Fig. 7: Curvature, torsion and tortuosity of the internal carotid artery centerline.

Figure 7 displays the evaluation of curvature, torsion and tortuosity applied to the centerline extracted from an internal carotid siphon.

C. Centerline framing: Frenet and parallel transport frames

The *Frenet frame* is a orthonormal coordinate reference frame computed along the line, carrying an intrinsic description of the local geometry. The unit vectors making up the reference frame have a strong connection with the concepts of curvature and torsion introduced in the previous section. Assuming that $\mathbf{c}(s)$ is at least three times differentiable, the Frenet frame is identified by the unit vectors *tangent* $\mathbf{t}_f$, *binormal* $\mathbf{b}_f$ and *normal* $\mathbf{n}_f$, respectively defined as

$$\begin{aligned} \mathbf{t}_f(s) &= \frac{\mathbf{c}\prime(s)}{\mid \mathbf{c}\prime(s) \mid}, \\ \mathbf{b}_f(s) &= \frac{\mathbf{c}\prime(s) \times \mathbf{c}\prime\prime(s)}{\mid \mathbf{c}\prime(s) \times \mathbf{c}\prime\prime(s) \mid}, \\ \mathbf{n}_f(s) &= \mathbf{b}_f(s) \times \mathbf{t}_f(s). \end{aligned} \tag{9}$$

Vectors $\mathbf{n}_f$ and $\mathbf{b}_f$ belong to the plane orthogonal to $\mathbf{t}_f$. At each point on the curve, $\mathbf{n}_f$ is directed toward the center of the osculating circle, while $\mathbf{b}_f$ is aligned with the normal to the osculating plane. In Figure 8 A, the Frenet frame computed along a centerline is shown. The Frenet frame is not defined when the curvature vanishes and by definition abruptly changes orientation when the direction of concavity of the curve changes. Figure 8 B shows an example of local osculating planes twisting around the curve due to a concavity change.

Although effective in accounting for the local geometry of a curve, due to its abrupt changes in orientation the Frenet frame cannot be employed as a reference frame for the evaluation or the comparison of circumferential positions around the centerline. For this purpose we resort to a different moving frame, the *parallel transport* frame [29]. The basic idea is to sweep an initial orthonormal coordinate frame along the line without being affected by torsion: at each point, the unit vectors making up the frame are rotated of the exact amount required by curvature, resulting in the least possible change in direction. In practice, given an initial frame at a point with parametric coordinate $\bar{s}$ (e.g. the Frenet frame in that point), featuring $\mathbf{t}(\bar{s})$, $\mathbf{n}(\bar{s})$ and $\mathbf{b}(\bar{s})$, the frame at $\bar{s}+ds$ is obtained by rotating the frame at $\bar{s}$ by an angle $\alpha_{\bar{s},\bar{s}+ds} = \mathbf{t}(\bar{s}) \angle \mathbf{t}(\bar{s}+ds)$ (i.e. the angle between the two successive tangent vectors) around the direction of the vector $\mathbf{t}(\bar{s}) \times \mathbf{t}(\bar{s}+ds)$. Such constructed parallel transport frame minimizes the twist of the moving frame as it is swept along the centerline, and as such it can be used for comparing angular positions around the centerline between different locations along the curve. Operatively, this is performed as in Figure 8, where the comparison between the orientation of two different planes identified by their normal is shown: the two normals are first transported along the centerline, and their orientation compared at a generic point (since the angle between the two parallel transported sets of normals is constant).

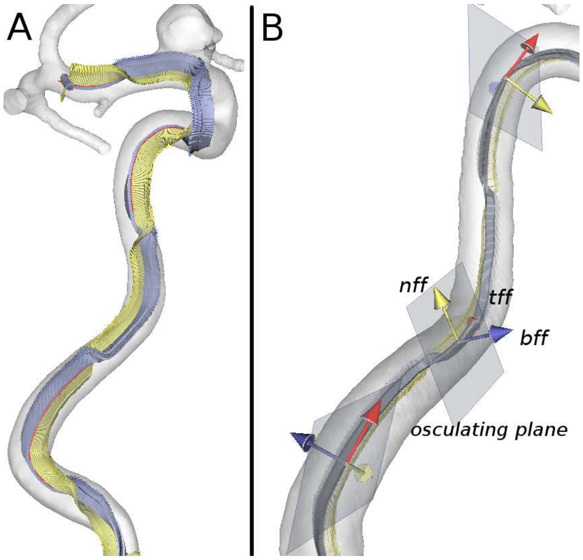

Fig. 8: A. Frenet frame along the internal carotid artery; B. detail of image A showing local osculating planes twisting around the centerline; $\mathbf{t}_f$, $\mathbf{n}_f$, $\mathbf{b}_f$ are respectively the tangent, normal and binormal unit vectors of the frame.

IV. ANALYSIS OF BIFURCATIONS

In the previous Section we faced the problem of providing tools for geometric characterization of vessels represented by centerlines, computed independently between endpoints. No information has been extracted yet on the topological relationship between centerlines representing difference branches of a vascular network and the related geometric characterization. Indeed, the availability of tools for the robust analysis of the geometry of bifurcations is of paramount importance for the applications addressed here, given the fact that bifurcations are locations where complex flow has a chance to develop, and that several vascular diseases exhibit focal effects precisely around bifurcations, e.g. atherosclerosis [30], [31] and aneurysmal disease of the cerebral circulation [32]–[35]. In the present Section we illustrate how it is possible to identify and characterize bifurcations from the current definition of centerlines and tubes.

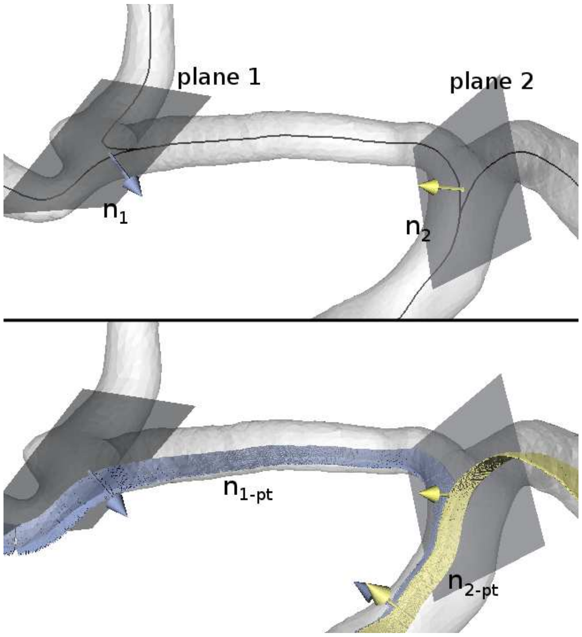

Fig. 9: Calculation of the angle between plane 1, defined by the normal vector $\mathbf{n}_1$, and plane 2, defined by normal vector $\mathbf{n}_2$, performed by parallel transport of the normal vectors along the centerlines, and by computation of the angle between the transported sets of unit vectors $\mathbf{n}_{1-\mathrm{pt}}$, $\mathbf{n}_{2-\mathrm{pt}}$ evaluated at a common location.

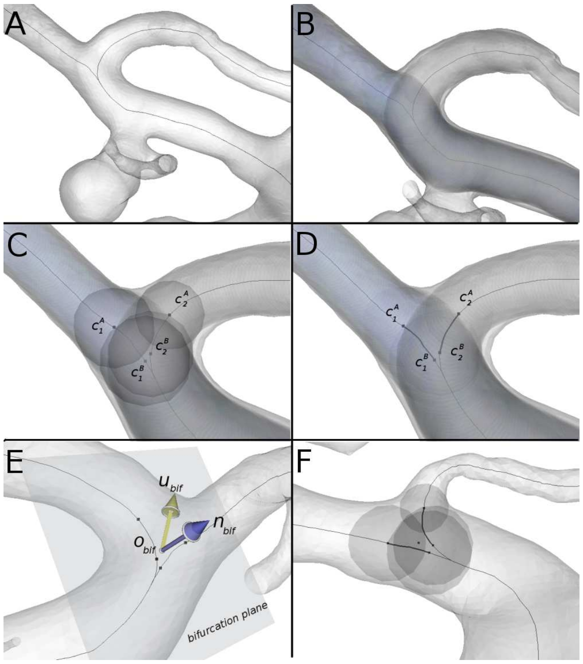

Fig. 10: Definition of the bifurcation reference system: A. 3D model of a bifurcating vessel and relative centerlines; B. intersecting tube surfaces generated from the two centerlines; C. identification of four reference points; D. centerline tracts relative to the bifurcation region, represented by thick tracts; E. bifurcation reference system: o_{bif}, origin, n_{bif}, bifurcation plane normal, u_{bif} downstream normal; F. example of bifurcation origin in case of bifurcating vessels of different sizes.

A. Identification

In our framework, the bifurcation is geometrically identified as the region preceding the location at which a centerline intersects the tube surface of another centerline and vice-versa. In other words, the location where two tubes graft into each other.

Let us consider, for the sake of concreteness, the bifurcating vessel shown in Figure 10A. Four reference points are identified on the two centerlines (see Figure 10, B-C.

1) $\mathbf{c}_1^A$ and $\mathbf{c}_2^A$ are the intersections of each centerline with the tube surface of the other;
2) $\mathbf{c}_1^B$ and $\mathbf{c}_2^B$ are the centers of the upstream maximal inscribed spheres touching $\mathbf{c}_1^A$ and $\mathbf{c}_2^A$.

These four points delimit a segment on each centerline which identifies the bifurcation region (Figure 10D). The center of mass $\mathbf{o}_{\mathrm{bif}}$ of the maximum inscribed spheres centered at the four reference points is taken as the origin of the bifurcation

$$\mathbf{o}_{\mathrm{bif}} = \frac{\sum_{i,j}\left(R_i^j\right)^2 \mathbf{c}_i^j}{\sum_{i,j}\left(R_i^j\right)^2}, \qquad i=1,2 \quad j=A,B, \tag{10}$$

where R_i^j are the radii of the maximal inscribed spheres associated with the centerline locations $\mathbf{c}_i^j$.

The *bifurcation plane* is then defined by the normal $\mathbf{n}_{\mathrm{bif}}$ to the polygon defined by the four reference points evaluated in $\mathbf{o}_{\mathrm{bif}}$. Since the four points are in general non-planar, the normal is evaluated as the bilinear interpolation in $\mathbf{o}_{\mathrm{bif}}$ of the normals to the corner triangles of the polygon. Last, the bifurcation reference frame is completed by defining the *downstream* direction $\mathbf{u}_{\mathrm{bif}}$ for the bifurcation as the normalized average of the vectors defined by the two reference points on each centerline. In Figure 10E all the components of the reference system are illustrated.

Notice that the approach based on the centerlines and tube functions yields a robust characterization of both Y- and T-shaped bifurcations. For instance, for two bifurcating vessels with a marked difference in size (see Figure 10F), the tube function of the smaller vessel slides along the outer wall of the bifurcation region, giving origin to a small intersection area and to reference points shifted towards the side of the larger vessel. On the other hand, the reference points located on the centerline of the larger vessel are associated to larger spheres and are therefore located in the neighborhood of the center of the vessel. By defining $\mathbf{o}_{\mathrm{bif}}$ with Equation (10) using the center of mass of the inscribed spheres as a weighting factor, the origin of the bifurcation results shifted towards the center of the main vessel, and the bifurcation normal will be less influenced by the reference point relative to the small branch.

B. Angle quantification

Once a bifurcation has been identified, each centerline $c_i(s)$ is split into the tracts $s \in \left[0, c_i^B\right]$ and $s \in \left[c_i^A, L_i\right]$, corresponding to the branches of the bifurcation, and $s \in \left[c_i^B, c_i^A\right]$, being L_i the length of the line. Tracts of different centerlines

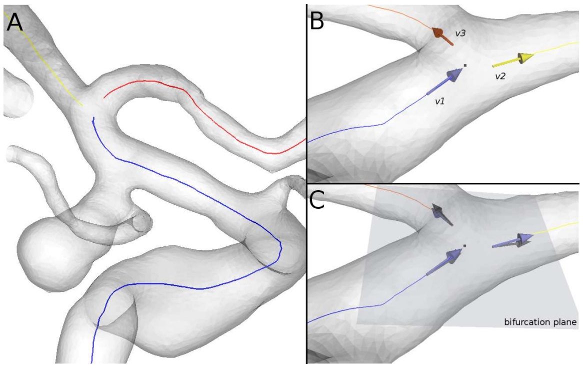

Fig. 11: A. Splitting of the bifurcating centerlines into branches; B. branch vectors; C. projection of the branch vectors on the bifurcation plane.

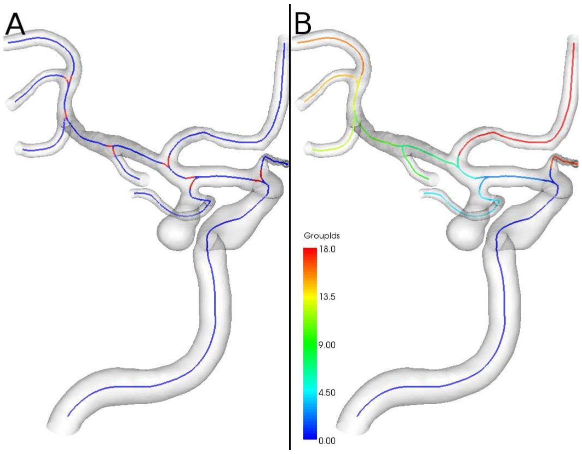

Fig. 12: Identification of the bifurcations (left) and splitting of the centerline into branches (right) in the case of a complex vascular network.

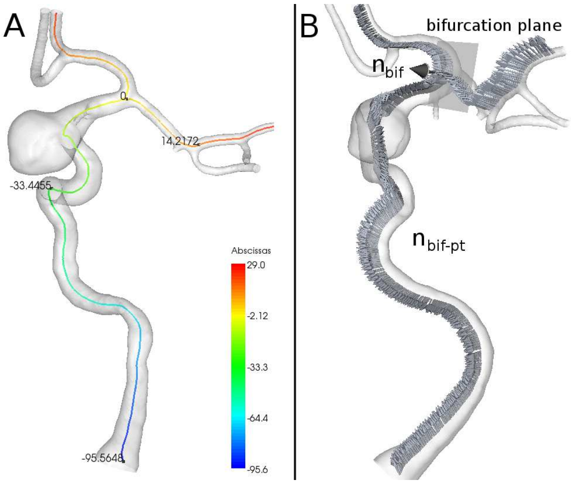

Fig. 13: Selection of a bifurcation as a landmark: the abscissa is set to zero in correspondence of the bifurcation point, while the bifurcation plane normal $\mathbf{n}_{\mathrm{bif}}$ is used to compute a parallel transport frame along the centerline.

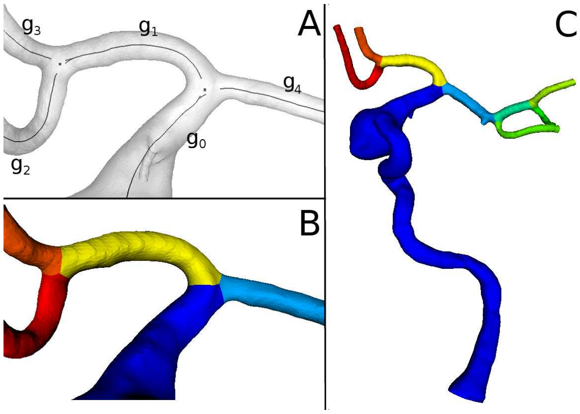

Fig. 14: A. Centerline network split into branches; B-C. splitting of the 3D model surface.

referred to the same branch are grouped based on whether they are mutually contained within their respective tube surfaces.

In order to characterize the directions of the branches relative to the the bifurcation, we associate a unit vector to each branch afferring or emanating from a bifurcation, capturing the direction of centerlines immediately upstream or downstream the bifurcation, as illustrated in Figure 11B. In order to estimate directions robustly, each branch vector is taken from (to) the relative reference point to (from) a point at a maximal inscribed sphere radius distance from it.

Once branch vectors are available, it is possible to quantify bifurcation angles. Each vector is split into its in-plane and out-of-plane components with respect to the bifurcation plane (see Figure 11C). The angles comprised by the in-plane and out-of-plane components can then be computed.

By detecting bifurcations in a vascular tree, the complete topology of the vascular network can be retrieved, as shown in Figure 12.

C. Comparative geometric analysis

When comparing the geometry of vascular segments from serial acquisitions or in patient populations, bifurcation origins can constitute important landmarks for comparative analysis of all geometric features (e.g. the distance of a lesion from a bifurcation, or the angular position of a lesion around the centerline with respect to the bifurcation normal).

For this purpose, centerlines are reparameterized setting the location of zero curvilinear abscissa $\mathbf{c}(s = 0)$ at the location where the centerline is closest to the bifurcation origin $\mathbf{o}_{\mathrm{bif}}$. Similarly, the parallel transport reference system for centerlines is generated by choosing as the initial normal $\mathbf{n}_1$ to be transported the bifurcation normal $\mathbf{n}_{\mathrm{bif}}$. This way, every orientation evaluated around the centerline can be given relative to the orientation of the bifurcation plane.

Figures 13A and B illustrate the choice of the ICA bifurcation as a landmark for both the abscissa and the parallel transport reference frame. These concepts will be then employed in Section V.

D. Surface splitting

Identification of individual branches on centerlines allows the decomposition of the 3D surface into equivalent branches.

As detailed above, once centerlines have been split into branches, the tracts belonging to the same branch i are grouped and denoted by g_i. For instance, in the case of the bifurcating vessel of Figure 14A, the tracts relative to the two parent branches are grouped into g_0 and g_1 respectively, while the terminal tracts are taken individually as g_2, g_3 and g_4. The tracts relative to the bifurcation region are not considered. Each group is then associated with the group function $\gamma_i(\mathbf{x})$ which is the union of the tube functions of the tracts composing the group.

Decomposition of the surface is carried out on the basis of $\gamma_i(\mathbf{x})$. In fact, we can operate a partition of $\mathcal{R}^3$, in which the i-th region is made up from points for which $\gamma_i(\mathbf{x})$ is lower than for the union of all the other groups, more formally

$$\Gamma_i = \left\{ \mathbf{x} \in R^3 : \gamma_i(\mathbf{x}) < \bigcup_{j \neq i} \gamma_j(\mathbf{x}) \right\} \tag{11}$$

In other words, Γ_i is the *region of influence* of the branch associated with the group function γ_i. The decomposition of the surface is performed according to the partition in Equation (11), where the boundaries of each region are the lines where $\gamma_i(\mathbf{x}) - \bigcup_{j\neq i} \gamma_j(\mathbf{x}) = 0$ In Figure 14B-C the resulting decomposition of the surface is shown. Due to the gap left in the bifurcation region, the boundaries meet within the bifurcationregion. The actual location of a splitting boundary depends from the relative size of the vessels, as represented by the tube functions.

Once the vascular network is split into branches, each segment is topologically equivalent to a cylinder. This simplifies its geometric characterization. For example, it is possible to robustly generate cross-sections of the vessel along the centerline, in order to evaluate their cross-sectional area [31] or shape factor (i.e. the ratio between the minimum and maximum width of the section). The step between two consecutive sections can be either set as a fixed distance along the centerline, or specified in terms of maximum inscribed spheres, which is a mean of measuring distances along centerlines which takes into account the local size of the vessel and results in shorter steps for smaller vessels. In Figure 15 sections spaced one and four maximal spheres apart for all three branches are depicted.

V. APPLICATIONS

In the previous sections we presented the fundamental building blocks of our geometric analysis framework. All of them are available within the VMTK open-source project. In this section, we present the actions of these tools on two concrete examples for the study of the geometric relationship of cerebral aneurysms with respect to their parent vessels, a topic that has been subject of interest in the literature [34], [36], [37]. The first application deals with aneurysms developing at terminal bifurcations, such as at the bifurcation of the middle cerebral artery. The second application deals with lateral aneurysms developing along the siphon of the internal carotid artery. Since aneurysm formation, growth and rupture are thought to be linked to the action of hemodynamic forces, the study of the geometric relationship between aneurysms and parent vessels is of primary importance for the identification of hemodynamic triggers of development and risk factors of rupture.

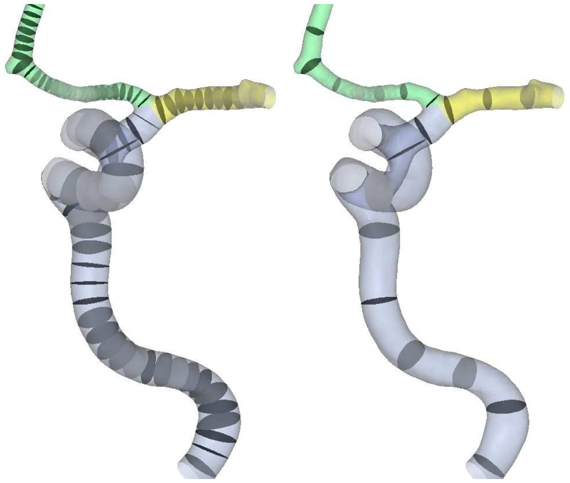

Fig. 15: Sections along the branches extracted at different steps, defined in terms of maximum inscribed spheres. Sections are spaced one (left) and four (right) maximal inscribed spheres apart.

A. Middle Cerebral Artery (MCA) terminal aneurysms

The localization of MCA aneurysms on the distal wall of the terminal bifurcation has been considered a possible evidence of the role of hemodynamics in aneurysm development, thought to be somehow related to the impact of blood on the apex wall. A quantitative analysis of the geometric configurations of these aneurysms with respect to the bifurcation where they develop could provide strong hints to understanding of the role of hemodynamics, especially if extended to large populations. In Figure 16A, a typical case of MCA terminal aneurysm is shown.

As described in the previous sections, the angle between the direction of branches can be computed by resorting to branch vectors. In order to generate a branch vector accounting for the orientation of the aneurysm neck, an additional centerline is generated with one endpoint on the distal wall of the aneurysm sac, as displayed in Figure 16B. Even if the aneurysm centerline does not account for the complex shape of the sac, it can represent the orientation of the neck with respect to the parent vessel.

The bifurcation region is then identified from the vessel centerlines and the bifurcation reference system is computed (Figure 16C). Bifurcation vectors are then computed in the two configurations, namely excluding and including the aneurysm centerline. Figure 16D shows branch vectors in the section configuration. Recalling the definition of reference points during the identification of a bifurcation, the base point of the aneurysm vector accounts for the location where the aneurysm is *grafted* on the parent vessel.

Given the branch vectors, the following geometric quantities are computed:

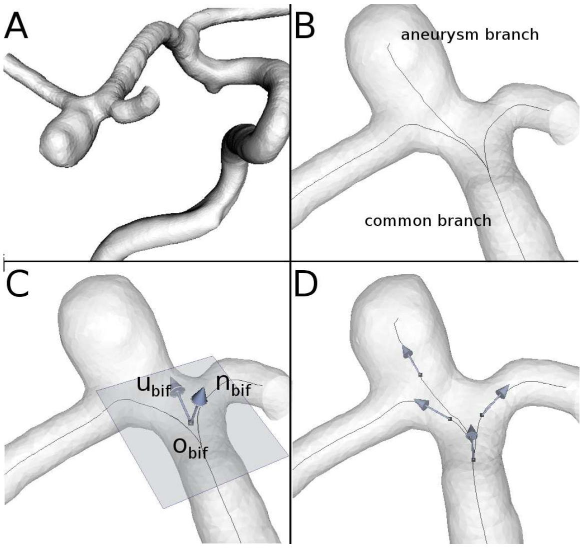

Fig. 16: A. 3D model of a terminal MCA aneurysm; B. centerlines of the parent vessel, daughter arteries and aneurysm sac; C. bifurcation reference system, computed considering the parent branch and the daughter arteries alone; D, bifurcation vectors for all branches originating from the bifurcation, including the aneurysm centerline.

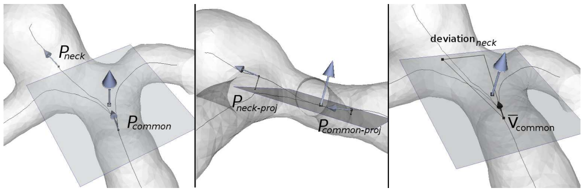

Fig. 17: Steps for the calculation of the deviation of the neck from the direction of the parent branch in the bifurcation plane. Left: P_{neck} and P_{common} are the base points of the respective bifurcation vectors; center: the projection on the bifurcation plane is shown; right: neck basepoint from the direction $\bar{V}_{\text{common}}$ of the parent artery is then computed.

- the relative orientations of all the branches (including the one relative to the aneurysm neck), obtained from the angles between the in-plane and out-of-plane branch vectors;
- the geometry of the sections of the parent branch, the daughter arteries and the aneurysm branch, extracted one maximum inscribed sphere away from the bifurcation and characterized using section-related parameters as area, minimum and maximum section diameters;
- the deviation of the aneurysm neck from the direction of the parent branch (see Figure 17).

More in detail, the latter quantity is determined as follows:

1) the base points of the aneurysm vector P_{neck} and the parent branch vector P_{common} (in Figure 17A) and their projection on the bifurcation plane $P_{\text{neck}-\text{proj}}$ $P_{\text{common}-\text{proj}}$ (in Figure 17B) are computed, as well as the projection of the parent branch vector on the bifurcation plane, $\overline{V}_{\text{common}}$, applied in $P_{\text{common}-\text{proj}}$;
2) the deviation $\text{deviation}_{\text{neck}}$ of the neck from the parent vessel direction is obtained as the distance of $P_{\text{neck}-\text{proj}}$ from the direction $\overline{V}_{\text{common}}$ (see Figure 17C); the direction of the $\text{deviation}_{\text{neck}}$ vector provides information on the deviation of the neck towards the smaller or the larger of the daughter arteries.

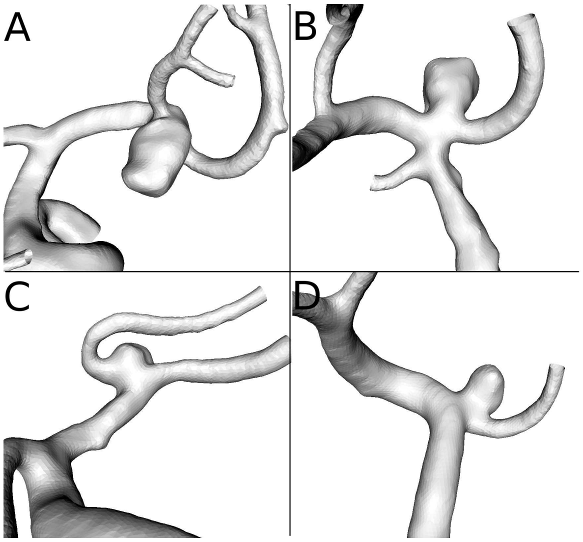

Fig. 18: 3D models of MCA terminal aneurysms used in the analysis.

TABLE I: Geometric data on four MCA aneurysms: section parameters. Notation: AR_L, section area ratio between largest daughter artery and parent artery; AR_S, section area ratio between smallest daughter artery and parent artery; AR, bifurcation area ratio between sum of daughter artery section areas and parent artery; A_{AN}, section area at aneurysm base point P_{neck}, in mm^2.

	AR_L	AR_S	AR	A_{AN}
A	0.59	0.39	1.05	21.23
B	1.08	0.65	1.68	10.61
C	0.61	0.35	0.95	10.13
D	1.29	0.28	1.56	7.28

Analogous operations can be performed to obtain the deviation of the neck perpendicularly to the bifurcation plane, the out-of-plane deviation (as in Figure 17B).

The quantities detailed above have been determined for four representative patient-specific models of MCA terminal aneurysms, extracted from the Aneurisk project database of RA models and shown in Figure 18. Results of the analysis are presented in Tables I, II, III, IV, V, where rows are reported in the same order as the models in Figure 18.

To attest the robustness of our methods to the segmentation strategy, three different models were generated from the RA imaging data of three MCA terminal aneurysms from the Aneurisk database: the model obtained by means of the level set segmentation and two additional models obtained through simple iso-surface extraction of the RA data at two user-defined thresholds, after the application of a gaussian filter on the image (with standard deviation 2 pixels) for the suppres-

TABLE II: Geometric data on four MCA aneurysms: in-plane aneurysm deviation. Notation: $\mathrm{dev_{in}}$, deviation of the aneurysm neck from the parent branch direction, in mm; $\mathrm{reldev_{in}}$ deviation of the aneurysm neck relative to the radius of the parent artery; $\mathrm{devside_{in}}$, side of deviation of the aneurysm neck, L, larger daughter, S, smaller daughter branch.

	$\mathrm{dev_{in}}$	$\mathrm{reldev_{in}}$	$\mathrm{devside_{in}}$
A	0.37	0.28	L
B	0.94	0.81	S
C	1.21	0.84	S
D	1.05	0.80	S

TABLE III: Geometric data on four MCA aneurysms: out-plane aneurysm deviation. Notation is analogous to Table II for out-of-plane quantities.

	$\mathrm{dev_{out}}$	$\mathrm{reldev_{out}}$	$\mathrm{devside_{out}}$
A	0.52	0.39	S
B	0.84	0.72	S
C	0.35	0.25	L
D	1.00	0.76	S

TABLE IV: Geometric data on four MCA aneurysms: in-plane angles. Notation (for conciseness, all vectors are mentioned in lieu of their in-plane components): γ, angle between parent branch vector and the downstream unit vector $\mathbf{u}_{\mathrm{bif}}$ of the bifurcation reference system; δ_1 and δ_2, angle between the parent branch vector and the largest and smallest daughter artery, respectively; α, angle between the parent branch and the aneurysm neck direction; $\delta_1\delta_2$, angle between daughter arteries, or bifurcation angle; $\delta_1\alpha$ and $\delta_2\alpha$, angle between the aneurysm neck direction and the largest and smallest daughter artery, respectively.

	γ	δ_1	δ_2	α	$\delta_1\delta_2$	$\delta_1\alpha$	$\delta 2\alpha$
A	15.12	62.39	86.34	22.67	148.73	39.72	109.00
B	1.81	61.87	74.80	67.92	136.68	129.79	6.88
C	11.95	54.83	95.47	4.70	150.29	59.53	90.76
D	1.00	48.26	91.35	43.76	139.61	92.02	47.59

TABLE V: Geometric data on four MCA aneurysms: out-plane angles. Notation is analogous to Table IV, where angles are evaluated between out-of-plane components of the mentioned vectors.

	γ	δ_1	δ_2	α	$\delta_1\delta_2$	$\delta_1\alpha$	$\delta 2\alpha$
A	21.50	17.84	36.87	66.66	19.03	48.82	29.79
B	0.66	6.56	2.94	0.66	3.62	5.89	2.27
C	1.16	2.72	15.93	6.21	18.65	3.49	22.14
D	11.34	18.75	8.02	20.19	10.73	38.94	28.21

TABLE VI: Comparison between in-plane branch angles of three MCA aneurysm models obtained with level set segmentation and iso-surface extraction at two user-defined thresholds. Notation: LS, level sets model, HT, higher threshold model, LT, lower threshold model. Notation for angles is same as Table IV.

	γ	δ_1	δ_2	α	$\delta_1\delta_2$	$\delta_1\alpha$	$\delta 2\alpha$
$\mathrm{A_{LS}}$	15.12	62.39	86.34	19.14	148.73	43.25	105.47
$\mathrm{A_{HT}}$	19.09	68.65	89.45	16.02	158.11	52.63	105.48
$\mathrm{A_{LT}}$	14.80	62.35	90.79	14.13	153.14	48.22	104.92
$\mathrm{B_{LS}}$	1.81	61.87	74.80	67.92	136.68	129.79	6.88
$\mathrm{B_{HT}}$	2.58	50.30	60.58	48.50	110.88	98.80	12.08
$\mathrm{B_{LT}}$	5.88	53.61	73.40	70.01	127.01	123.62	3.39
$\mathrm{E_{LS}}$	3.21	90.80	69.41	9.31	160.21	81.48	78.73
$\mathrm{E_{HT}}$	6.32	72.53	86.43	14.59	158.96	57.94	101.02
$\mathrm{E_{LT}}$	4.08	77.36	72.30	48.51	149.66	125.87	23.79

TABLE VII: Comparison between out-of-plane branch angles of three MCA aneurysm models obtained with level set segmentation and iso-surface extraction at two user-defined thresholds. Notation: LS, level sets model, HT, higher threshold model, LT, lower threshold model. Notation for angles is same as Table V.

	γ	δ_1	δ_2	α	$\delta_1 - \delta_2$	$\delta_1 - \alpha$	$\delta 2 - \alpha$
$\mathrm{A_{LS}}$	21.50	17.84	36.87	64.89	19.03	47.05	28.02
$\mathrm{A_{HT}}$	27.95	11.72	28.22	58.82	16.50	47.10	30.61
$\mathrm{A_{LT}}$	27.26	12.25	26.08	68.68	13.83	56.43	42.60
$\mathrm{B_{LS}}$	0.66	6.56	2.94	0.66	3.62	5.89	2.27
$\mathrm{B_{HT}}$	3.70	8.69	3.83	4.41	4.86	4.27	0.58
$\mathrm{B_{LT}}$	2.46	8.89	4.75	2.46	4.14	6.43	2.29
$\mathrm{E_{LS}}$	9.78	34.25	6.73	25.10	27.53	59.36	31.83
$\mathrm{E_{HT}}$	5.87	33.24	1.88	20.99	31.36	54.24	22.88
$\mathrm{E_{LT}}$	5.19	30.83	6.45	5.19	37.28	25.64	11.65

sion of noise. For each model, centerlines and the bifurcation vectors were extracted and in-plane and out-of-plane angles between the branches were computed as described. Results are reported in Tables VI and tab:22, and show excellent robustness of the parameters to the segmentation method. However, in some cases, iso-surface extraction with user-specified thresholds can produce changes in the geometry of the surface with the inclusion of spurious structures potentially leading to changes in the geometric parameters (see case E). For this reason, we argue for the adoption a robust segmentation method in order to obtain reliable geometric parameters.

B. Internal Carotid Artery (ICA) lateral aneurysms

In this section, we present the extension of what presented for terminal aneurysm to the analysis of lateral aneurysms, which are not associated to a bifurcation. These aneurysms typically arise in correspondence of sharp bends, as it is the case along the carotid siphon.

Figure 19 shows the cases that have been retrieved from the Aneurisk project data base, and that will be employed in this section. The ICA and the aneurysm centerlines are also displayed. Regarding the latter, it is worth noting that, even if the position of the centerline endpoint on the aneurysm sac obviously influences the aneurysm centerline trajectory, the orientation of the centerline through the neck is fairly stable with respect to the selection of the endpoints (Figure 19D), which ensures that the direction of the aneurysm neck is robust to this choice.

Once the two centerlines are extracted, we consider the location of the aneurysm neck as a bifurcation, which we refer to as *aneurysm bifurcation*. We can then characterize the aneurysm bifurcation using the geometric quantities described in the

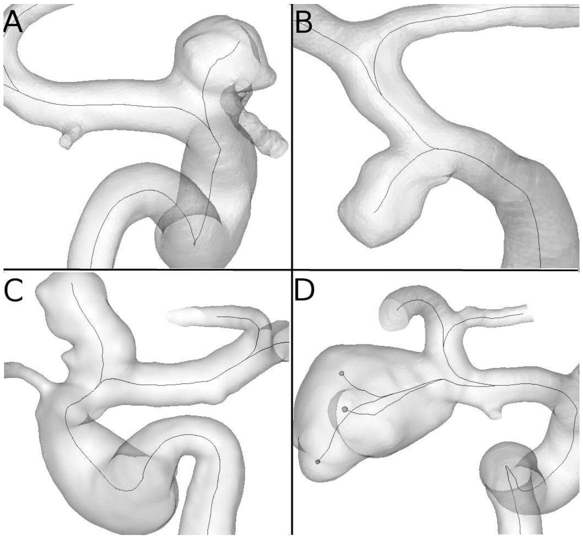

Fig. 19: A,B,C,D. 3D models of ICA lateral aneurysms; D. robustness of the orientation of the centerline through the neck with respect to the selection of the distal centerline endpoint on the aneurysm.

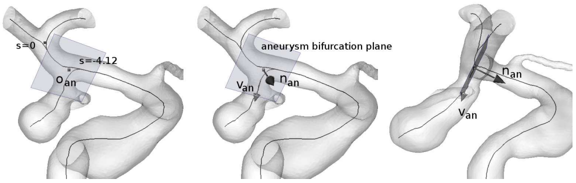

Fig. 20: Extraction of the position of the neck along the siphon centerline as the origin of the aneurysm bifurcation $\mathbf{o}_{\mathrm{an}}$; the bifurcation plane normal $\mathbf{n}_{\mathrm{an}}$ and the direction of the aneurysm branch vector $\mathbf{v}_{\mathrm{an}}$ are determined.

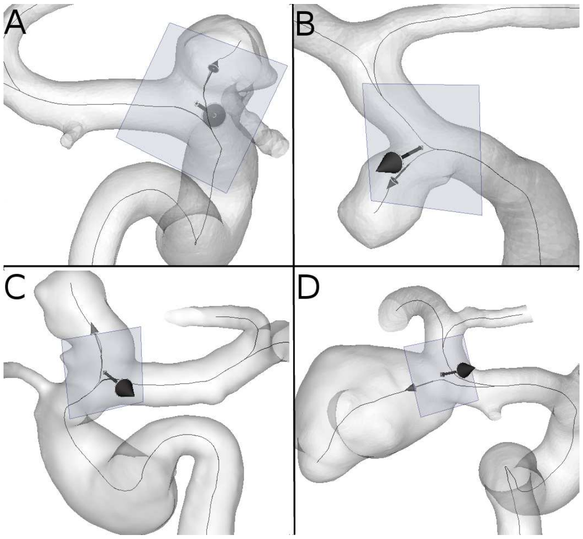

Fig. 21: Four cases of ICA lateral aneurysms, shown with the respective aneurysm bifurcation planes and vectors.

previous section, namely the bifurcation area, the aneurysm bifurcation reference system and the bifurcation vectors. By means of the reference system, the position and orientation of the neck with respect to the ICA are quantified. The origin of the reference system $\mathbf{o}_{\mathrm{an}}$ accounts for the location of the aneurysm neck along the carotid siphon, the normal to the aneurysm bifurcation plane $\mathbf{n}_{\mathrm{an}}$ represents the orientation of the plane on which the aneurysm develops in the neck region, and the branch vector relative to the aneurysm centerline $\mathbf{v}_{\mathrm{an}}$ identifies the main direction of the sac immediately distal to the neck.

In Figure 20 we depict the details of the aneurysm neck region for one of the models together with the relative geometric features. Assuming the ICA terminal bifurcation as a landmark, curvilinear abscissa of the point $\mathbf{o}_{\mathrm{an}}$ allows us to quantify the position of the aneurym along the siphon, while the aneurysm bifurcation plane locally identifies the aneurysm centerline direction in the neck region.

Figure 21 shows the geometric characterization of four lateral aneurysms. The description of the local geometry of the carotid siphon, i.e. the local plane of curvature of the parent vessel, is performed by means of the Frenet frame defined along the ICA centerline. At each point, the binormal vector $\mathbf{b}_f\left(s\right)$ identifies the osculating plane where the ICA locally lies (see Figure 10A and B); consequently the osculating plane calculated at the point $\mathbf{o}_{\mathrm{an}}$ defines the orientation of the parent vessel in the proximity of the aneurysm neck.

The comparison between the orientation of the local ICA osculating plane and the aneurysm bifurcation plane, i.e. between $\mathbf{b}_f$ and $\mathbf{n}_{\mathrm{an}}$, ultimately represents the angular orientation of the aneurysm with respect to its parent vessel. This is a significant quantity, as it assesses whether the aneurysm developed on the outer wall of a bend and with which orientation with respect to the bend itself. The quantity bears a direct connection with hemodynamics forces originating from flow in bent vessels. In Table VIII, quantitative information on the location and orientation of the lateral aneurysms depicted in Figure 21 is reported.

The sequence in Figure 22 illustrates the steps needed to obtain the angle between the ICA osculating plane at any point of the ICA and the aneurysm bifurcation plane, performed using the parallel transport technique, as presented in Section III. This allows to evaluate the angular orientation of the aneurysm with respect to any osculating plane, e.g. upstream the neck. This is again a hemodynamically relevant quantity, as it accounts for the role of upstream geometry in determining hemodynamic forces at the neck region.

More complete quantitative analyses of the geometry of ICA and its possible relations with the presence of aneurysms will be presented in future work [38], [39].

VI. CONCLUSION

In this paper, we presented a complete framework for robust characterization of vascular geometry, and we provided a description of the application of the framework to the case of cerebral aneurysms.

Thanks to the objective criteria introduced in our framework, and to the availability of the tools as part of the Vascular Modeling Toolkit, quantitative geometric features are readily

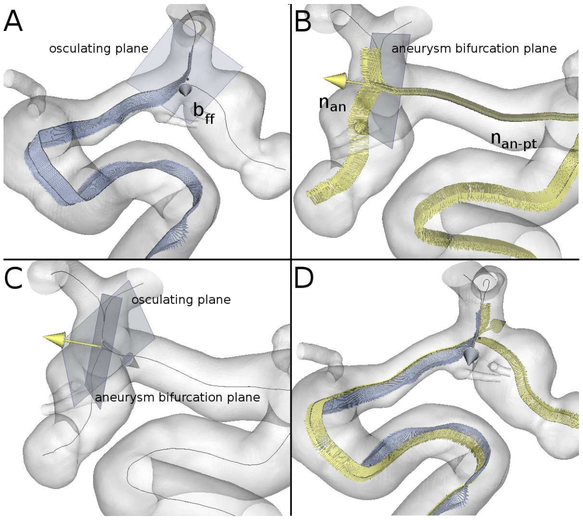

Fig. 22: Definition of the orientation of the aneurysm neck with respect to the local parent vessel geometry: A. osculating plane of the parent artery at the aneurysm site; B. aneurysm bifurcation normal $\mathbf{n}_{\text{an}}$ parallel transported along the siphon centerline; C. comparison between the aneurysm bifurcation plane and the siphon osculating plane at the aneurysm site; D. computation of the angle between the two planes.

TABLE VIII: Position and orientation of the neck of the ICA aneurysm models shown as A,B,C,D in Figure 19. Notation: $\text{abscissa}_{\mathbf{neck}}$, aneurysm neck abscissa with respect to the ICA terminal bifurcation (negative since the ICA bifurcation is downstream the ICA) in mm; $\text{orientation}_{\mathbf{neck}}$, aneurysm neck orientation with respect to the local ICA osculating plane.

	$\text{abscissa}_{\mathbf{neck}}$	$\text{orientation}_{\mathbf{neck}}$
A	-11.94	47.86
B	-4.70	31.66
C	-12.40	43.36
D	-3.90	20.79

available from imaging data, and can be easily employed at a large scale for explorative studies, clinical trials and clinical routine, in order to elucidate and exploit the role of geometry and hemodynamics in vascular disease.

ACKNOWLEDGMENTS

The Aneurisk project is a joint research project of the Center for Modeling and Scientific Computing (MOX) of the Politecnico di Milano, Milan (Italy), the Mario Negri Institute for Pharmacological Research, Bergamo (Italy) and the Ca' Granda Hospital, Milan (Italy), supported by Siemens Medical Italia and Fondazione Politecnico, which we gratefully acknowledge.

REFERENCES

[1] C. Caro, D.J.Doorly, M. Tarnawski, K. Scott, Q. Long, and C. Dumoulin, "Non-planar curvature and branching of arteries and non-planar-type flow," *Proc Roy Soc*, vol. 452, no. 1944, pp. 185–197, 1996.

[2] K. Perktold, R. Peter, M. Resch, and G. Langs, "Pulsatile non-newtonian blood flow in three-dimensional carotid bifurcation models: a numerical study of flow phenomena under different bifurcation angles," *J Biomed Eng*, vol. 13, no. 6, pp. 507–1, 1991.

[3] S. Sherwin, O. Shah, D. Doorly, M. McLean, N. Watkins, C. Caro, J. Peiro, M. Tarnawski, and C. Dumoulin, "Visualization and computational study of flow at model planar and non-planar end-to-side arterial bypass graft," *J Physiol-London*, vol. 504P, pp. P44–P44, 1997.

[4] S. Sherwin, O. Shah, D. Doorly, J. Peiro, Y. Papaharilaou, N. Watkins, C. Caro, and C. Dumoulin, "The influence of out-of-plane geometry on the flow within a distal end-to-side anastomosis," *J Biomech Eng*, vol. 122, no. 1, pp. 86–95, 2000.

[5] U. Schulz and P. Rothwell, "Major variation in carotid bifurcation anatomy: a possible risk factor for plaque development?" *Stroke*, vol. 32, no. 11, pp. 2522–2529, 2001.

[6] A. Malek, S. Alper, and S. Izumo, "Hemodynamic shear stress and its role in atherosclerosis," *JAMA*, vol. 282, no. 21, pp. 2035–2042, 1999.

[7] Y. Hoi, H. Meng, S. Woodward, B. Bendok, R. Hanel, L. Guterman, and L. Hopkins, "Effects of arterial geometry on aneurysm growth: three-dimensional computational fluid dynamics study," *J Neurosurg*, vol. 101, no. 4, pp. 676–681, 2004.

[8] G. Foutrakis, H. Yonas, and R. Sclabassi, "Saccular aneurysm formation in curved and bifurcating arteries," *Am J Neuroradiol*, vol. 20, no. 7, pp. 1309–1317, 1999.

[9] M. Friedman, "Variability of 3d arterial geometry and dynamics and its pathologic implications," *Biorheology*, pp. 513–517, 2002.

[10] M. Friedman, O. Deters, F. Mark, C. Bargeron, and G. Hutchins, "Arterial geometry affects hemodynamics. a potential risk factor for atherosclerosis," *Atherosclerosis*, vol. 46, pp. 225–231, 1983.

[11] P. O'Flynn, G. O'Sullivan, and A. Pandit, "Methods for three-dimensional geometric characterization of the arterial vasculature," *Ann Biomed Eng*, vol. 35, no. 8, pp. 1368–1381, 2007.

[12] C. Taylor, M. Draney, J. Ku, D. Parker, B. Steele, K. Wang, and C. Zarins, "Predictive medicine: computational techniques in therapeutic decision making," *Comp Aided Surg*, vol. 4, no. 5, pp. 231–247, 1999.

[13] J. Cebral, M. Castro, S. Appanaboyina, C. Putman, D. Millan, and A. Frangi, "Efficient pipeline for image-based patient-specific analysis of cerebral aneurysm hemodynamics: technique and sensitivity," *IEEE Trans Med Imaging*, vol. 24, no. 4, pp. 457–467, 2005.

[14] J. Cebral, M. Castro, J. Burgess, R. Pergolizzi, M. Sheridan, and C. Putman, "Characterization of cerebral aneurysms for assessing risk of rupture by using patient-specific computational hemodynamics models," *AJNR*, vol. 26, no. 10, pp. 2550–2559, 2005.

[15] M. Castro, C. Putman, and J. Cebral, "Computational fluid dynamics modeling of intracranial aneurysms: effects of parent artery segmentation on intra-aneurysmal hemodynamics," *AJNR*, vol. 27, no. 8, pp. 1703–1709, 2006.

[16] L. Antiga and D. A. Steinman, "The vascular modeling toolkit," *http://www.vmtk.org*, Last accessed Oct 3, 2008.

[17] J. Sethian, Ed., *Level Set Methods and Fast Marching Methods*. 2nd Edition Cambridge University Press, 1999.

[18] J. Sethian, "A fast marching level set method for monotonically advancing fronts," *Proc Nat Acad Sci*, vol. 93, no. 4, pp. 1591–1595, 1996.

[19] L. Antiga, B. Ene-Iordache, and A. Remuzzi, "Computational geometry for patient-specific reconstruction and meshing of blood vessels from mr and ct angiography," *IEEE Trans Med Imaging*, vol. 22, no. 5, pp. 674–684, 2003.

[20] T. Dey and W. Zhao, "Approximate medial axis as a voronoi subcomplex," *Proceedings of the 7th ACM Symposium of Solid Modeling Applications*, pp. 356–366, 2002.

[21] N. Amenta, S. Choi, and R. Kolluri, "The power crust, unions of balls and the medial axis transform," *Computational Geometry: Theory and Applications*, vol. 19, no. 2, pp. 127–153, 2001.

[22] T. Dey and W. Zhao, "Approximating the medial axis from the voronoi diagram with a convergence guarantee," *Algorithmica*, vol. 38, no. 1, pp. 179–200, 2003.

[23] L. Antiga and D. Steinman, "Robust and objective decomposition and mapping of bifurcating vessels," *IEEE Trans Med Imaging*, vol. 23, no. 6, pp. 704–713, 2004.

[24] K. Lee, K.H.Parker, C. Caro, and S. Sherwin, "The spectral/hp element modeling of steady flow in non-planar double bends," *Int J Numer Meth Fluids*, vol. 00, pp. 1–16, 2006.

[25] E. Bullitt, G. Gerig, S. Pizer, W. Lin, and S. Aylward, "Measuring tortuosity of the intracerebral vasculature from mra images," *IEEE Trans Med Imaging*, vol. 22, no. 9, pp. 1163–1171, 2003.

[26] M. Poullis, R. Warwick, A. Oo, and R. Poole, "Ascending aortic curvature as an independent risk factor for type a dissection and ascending aortic aneurysm formation: a mathematical model," *Eur J Cardiothorac Surg*, vol. 33, no. 6, pp. 995–1001, 2008.

[27] H. Zhu, Z. Ding, R. Piana, T. Gehrig, and M. Friedman, “Cataloguing the geometry of the human coronary arteries: A potential tool for predicting risk of coronary artery disease,” *Int J Cardiol*, vol. Epub ahead of print, 2008.

[28] S. V. L.M. Sangalli, P. Secchi and A. Veneziani, “Efficient estimation of 3-dimensional centerlines of inner carotid arteries and their curvature functions by free knot regression splines,” vol. 2008, submitted, p. available at www.mathcs.emory.edu.

[29] R. Bishop, “There is more than one way to frame a curve,” *American Mathematical Monthly*, vol. 82, no. 3, pp. 246–251, 1975.

[30] J. Thomas, L. Antiga, S. Che, J. Milner, D. Steinman, J. Spence, B. Rutt, and D. Steinman, “Variation in the carotid bifurcation geometry of young versus older adults: implications for geometric risk of atherosclerosis,” *Stroke*, vol. 36, no. 11, pp. 2450–2456, 2005.

[31] S. Lee, L. Antiga, and D. S. J.D. Spence, “Geometry of the carotid bifurcation predicts its exposure to disturbed flow,” *Stroke*, vol. 39, no. 8, pp. 2341–2347, 2008.

[32] T. Ingebrigtsen, M. Morgan, K. Faulder, L. Ingebrigtsen, T. Sparr, and H. Schirmer, “Bifurcation geometry and the presence of cerebral artery aneurysms,” *J Neurosurg*, vol. 101, no. 1, pp. 108–113, 2004.

[33] H. Kasuya, T. Shimizu, K. Nakaya, A. Sasahara, T. Hori, and K. Takakura, “Angles between a1 and a2 segments of the anterior cerebral artery visualized by three dimensional computed tomographic angiography and association of anterior communicating artery aneurysms,” *Neurosurgery*, vol. 45, no. 1, pp. 89–93, 1999.

[34] T. Sadatomo, K. Yuki, K. Migita, E. Taniguchi, Y. Kodama, and K. Kurisu, “The characteristics of the anterior communicating artery aneurysm complex by three-dimensional digital subtraction angiography,” *Neurosurg Rev*, vol. 29, no. 3, pp. 201–207, 2006.

[35] W. van Rooij, M. Sluzewski, and G. Beute, “Internal carotid bifurcation aneurysms: frequency, angiographic anatomy and results of coiling in 50 aneurysms,” *Neuroradiology*, vol. 50, no. 7, pp. 583–587, 2008.

[36] T. Sadatomo, K. Yuki, K. Migita, E. Taniguchi, Y. K. Y, and K. Kurisu, “Evaluation of relation among aneurysmal neck, parent artery and daughter arteries in middle cerebral artery aneurysms, by three-dimensional digital subtraction angiography,” *Neurosurg Rev*, vol. 28, no. 3, pp. 196–200, 2005.

[37] T. Sadatomo, K. Yuki, K. Migita, E. Taniguchi, Y. Kodama, and K. Kurisu, “Morphological differences between ruptured and unruptured cases in middle cerebral artery aneurysms,” *Neurosurgery*, vol. 62, no. 3, pp. 602–609, 2008.

[38] M. Piccinelli, S. Bacigaluppi, E. Boccardi, B. Ene-Iordache, A. Remuzzi, A. Veneziani, and L. Antiga, “Influence of internal carotid artery geometry on aneurysm location and orientation: A computational geometry study,” 2008, submitted, available at www.mathcs.emory.edu.

[39] L. Sangalli, P. Secchi, S. Vantini, and A. Veneziani, “A case study in explorative functional data analysis: geometrical features of the internal carotid artery,” vol. 2008, submitted, p. available at www.mathcs.emory.edu.